Abnormal sign reversal of the fieldlike spin-orbit torque in Pt/Ni/Py with an ultrathin Ni spacer

Zishuang Li,[1] Wenqiang Wang,[1] Xiang Zhan,[1] Haozhe Wang,[1] Kaiyuan Zhou,[1]
Tiejun Zhou,[2,*] and Ronghua Liu[1,3,†]

[1]*National Laboratory of Solid State Microstructures, School of Physics and Collaborative Innovation Center of Advanced Microstructures, Nanjing University, Nanjing 210093, China*

[2]*Centre for Integrated Spintronic Devices, School of Electronics and Information, Hangzhou Dianzi University, Hangzhou 310018, China*

[3]*National Key Laboratory of Spintronics, Nanjing University, Suzhou 215163, China*

(Received 14 February 2023; revised 30 July 2024; accepted 31 July 2024; published 16 August 2024)

The magnetization manipulation by spin-orbit torques (SOTs) in nonmagnetic-metal (NM)–ferromagnet (FM) heterostructures has provided great opportunities for spin devices. Besides the conventional spin Hall effect (SHE) in heavy metals with strong spin-orbit coupling, the orbital currents have been proposed as another promising approach to generate strong SOTs. Here, we systematically study the SOT efficiency and its dependence on the FM thickness and different NM–FM interfaces in two prototypical Pt/Py and Ta/Py systems by inserting an ultrathin magnetic layer (ML), (0.4-nm-thick ML = Co, Fe, and Ni). The dampinglike (DL) torque efficiency ξ_{DL} is significantly enhanced by inserting ultrathin ML layers. Moreover, the Ni insertion results in a sign change of the fieldlike (FL) torque in Pt/Py and substantially reduces ξ_{DL} in Ta/Py. These results are likely related to the additional spin currents generated by combining the orbital Hall effect in the NM and orbital-to-spin conversion in the ML insertion layer and/or their interfaces, especially for the Ni insertion. Our results demonstrate that inserting ultrathin ML can effectively manipulate the strength and sign of the SOTs, which would be helpful for spintronics applications.

DOI: 10.1103/PhysRevB.110.064419

I. INTRODUCTION

Current-induced spin-orbit torques (SOTs) in NM–FM heterostructures have emerged as a promising approach for electric control of magnetization reversal to achieve energy-efficient SOT-magnetoresistive random access memory (SOT-MRAM) and compensation of the intrinsic magnetic damping for self-sustained nano-oscillator [1–10]. The foundation of these SOTs in bilayers is commonly associated with the spin Hall effect (SHE) in the NM layer with strong spin-orbit coupling (SOC) [11] and/or interfacial Rashba-Edelstein effect (iREE) [12,13] at the NM–FM interface with an enhanced interfacial SOC (iSOC) due to the inversion symmetry breaking. Under an in-plane electric field along the longitudinal direction of NM–FM bilayers, an out-of-plane spin current with transverse spin polarization and a net spin accumulation near the interface can be generated by SHE and iREE. These generated spin currents flow into the FM layer through the interface, consequently applying torques on magnetization via the spin-transfer mechanism. The net spin polarization due to the interfacial spin accumulation exerts torques on the adjacent magnetization via the exchange interaction. Notably, recent theoretical and experimental works have shown that the orbital current, the flow of orbital angular momentum perpendicular to the charge current, can be generated by an electric field in a broader range of materials even without the requisition of SOC. Termed the orbital Hall effect [14,15], the currents differ from their spin counterparts as they cannot couple directly to the magnetization. Before exerting torque on magnetization, the orbital currents must be converted into spin currents via SOC in the NM, FM, and/or interface.

Based on torque and magnetization orientations, these spin-current generated SOTs are distinctly classified as dampinglike (DL) torque [$\boldsymbol{\tau}_{DL} \propto \mathbf{m} \times (\mathbf{m} \times \boldsymbol{\sigma})$] and fieldlike (FL) torque [$\boldsymbol{\tau}_{FL} \propto (\mathbf{m} \times \boldsymbol{\sigma})$] [16,17]. In principle, the DL and FL torques arise from the absorption of the spin-current component transverse to magnetization $\mathbf{m}$ and the reflection of spin current with some spin rotation, respectively. In addition, besides the spin-current generation mechanisms mentioned above, the high interfacial transparency is also vital to achieving efficient magnetization manipulation for the development of low-energy consumption spintronic devices because the effective DL torque efficiency is given by $\xi_{DL} = T_{int}\theta_{sh}$, where T_{int} signifies the interfacial spin transparency and $\theta_{sh} = (2e/\hbar)j_s/j_c$ denotes the charge-to-spin current-conversion efficiency, known as the spin Hall angle. Employing a simplified drift-diffusion analysis [16,17], the spin current diffuses into the adjacent FM layer via the mediation of electrons and diminishes sharply near the NM–FM interface due to spin backflow (SBF) and spin memory loss (SML) [18] ($T_{int} = T_{int}^{SBF} \times T_{int}^{SML}$). According to the SOT-generation mechanisms above, it is a feasible scheme to achieve a high θ_{sh} and/or a large T_{int} for a highly efficient manipulation of magnetization in practical spin devices.

Previously, much effort has been contributed to exploring high SOT efficiency through exploring spin-source materials with high intrinsic bulk θ_{sh} and tailoring the interface

*Contact author: tjzhou@hdu.edu.cn
†Contact author: rhliu@nju.edu.cn

 ©2024 American Physical Society

with enhanced spin transmissivity and substantial interfacial SOTs [10,19,20]. Besides the extensively studied heavy metals (HMs) with strong SOC, such as Pt [18,21], Ta [2,5,22], and W [23,24], other materials, including the topological insulator Bi_xSe_{1-x} [25], $Bi_{1-x}Sb_x$ [26], and the highly conductive $Pt_{1-x}Au_x$ [27] alloys have been proven to exhibit high θ_{sh} or low-power consumption. On the other hand, interface engineering, e.g., insertion of ultrathin nonmagnetic layer like Hf [28], Mo [29], Cu [23,30,31], or two-dimensional van der Waals material $MoTe_2$ [32] between the HM and FM layers, oxygen-induced interface orbital hybridization [5], interfacial H^+ and O^{2-} ion manipulations [33], utilization of antiferromagnetic (or paramagnetic) insulating NiO or CoO_x thin layer [34–37], and magnetic metal spacer layer [38,39], has also been explored intensely. Several different mechanisms exist for these interface engineering methods (e.g., additional interface-generated SOTs, enhancing interfacial spin transparency, and orbital-to-spin current conversion) to enhance SOT efficiency. The experimentally quantitative measurement of the DL and FL torque efficiencies and identification of the underlying mechanisms in two prototypical Pt- and Ta-based systems are crucial for practical spintronics applications.

In this study, we present an investigation into the SOT efficiency dependence of the prototypical Pt/Py on different Pt–FM interfaces via inserting an ultrathin magnetic layer (ML = 0.4-nm-thick Co, Fe, and Ni) sandwiched between Pt and Py layers and Ta/Ni(0.5 nm)/Py, using spin-torque ferromagnetic resonance (ST-FMR) technique with varying thickness of Py. Notably, the dampinglike torque efficiency ξ_{DL} is enhanced by 21% with Co, 43% with Fe, and 33% with Ni insertion layers. In contrast to the Pt/Py with a negligible fieldlike torque $\xi_{FL} \sim -0.002$, the insertion of an ultrathin magnetic layer results in a considerable $|\xi_{FL}| \sim 0.016-0.023$ for Fe, and Co, and its sign reversal for the Ni insertion system ($\xi_{FL} \sim 0.011$). For Ta/Ni/Py system, both ξ_{FL} and ξ_{DL} are significantly suppressed by inserting a 0.4-nm-thick Ni spacer but do not change their signs. Beyond the conventional SHE-generated spin currents observed in the HM, our results suggest the potential existence of spin currents originating from the conversion of orbital currents to spin currents via the orbital Hall effect (OHE) within the NM layer and SOC within the FM layer, especially for the Ni insertion systems.

II. EXPERIMENTAL DETAILS

Multilayer films with the structure of Pt(6)/Py(t), Pt(6)/ML (0.4)/Py(t) (ML = Co, Fe, and Ni) (number in parentheses is thickness in nanometers) are deposited on annealed Al_2O_3 substrate with (0001) orientation by dc magnetron sputtering at room temperature. A 2-nm-thick MgO covers all multilayers to prevent oxidization in the air. To determine the SOT efficiency from the total ferromagnetic-layer thickness (t_{FM}^{tot}) dependence of the ST-FMR signal, we vary the Py thickness t from 3 to 8 nm for the Pt/Py, Pt/Co/Py, and Pt/Fe/Py and from 3 to 10 nm for the Pt/Ni/Py. All the samples are patterned into 5-μm × 8-μm stripes with two top electrodes of Au (80 nm) for ST-FMR measurement, as shown in Fig. 1(a). For the ST-FMR measurement, an in-plane external field H is applied at an angle of $\varphi = 30^\circ$ and $\varphi = 210^\circ$ from the longitudinal direction of the stripes. To better eliminate the influence of experimental errors on the effective demagnetization field $4\pi M_{eff}$ and linewidth ΔH, we used the average value of two directions to analyze all the data.

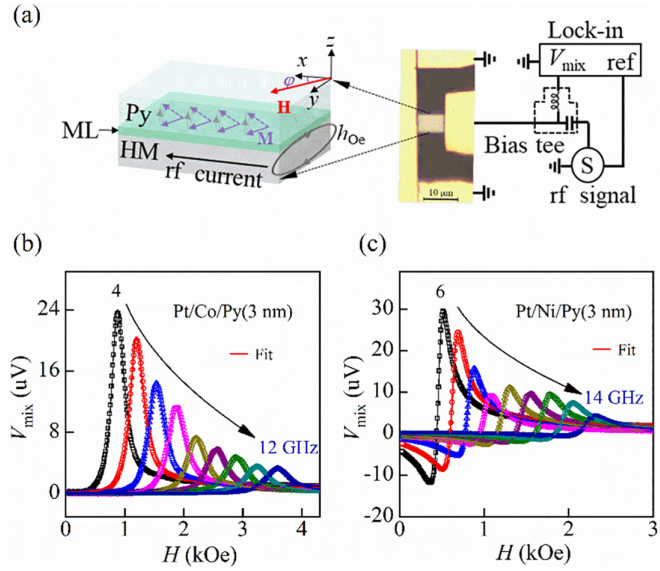

FIG. 1. (a) Left: Illustration of the stack structure of multilayer, coordinate system, and magnetization dynamics in the ST-FMR measurement. Right: schematic diagram of the ST-FMR setup. (b), (c) The representative ST-FMR spectra V_{mix} obtained with the excitation frequencies from $f = 4$ to 12 GHz and $f = 6$ to 14 GHz with a step of 1 GHz at $\varphi = 30^\circ$ for (b) Pt(6)/Co(0.4)/Py(3) and (c) Pt(6)/Ni(0.4)/Py(3) samples, respectively. The solid lines are the fitting results with Eq. (1).

III. RESULTS AND DISCUSSION

A. Spin-torque efficiencies in Pt-based trilayers

Figures 1(b) and 1(c) show the representative ST-FMR spectra of Pt(6)/Co(0.4)/Py(3) and Pt(6)/Ni(0.4)/Py(3) samples with excitation frequencies from 4 to 12 GHz and 6 to 14 GHz, respectively, at $\varphi = 30^\circ$. The obtained V_{mix} signal is fitted using a Lorentzian function [1,4,7]:

$$V_{mix} = V_s \frac{\Delta H^2}{[(H - H_{res})^2 + \Delta H^2]} + V_A \frac{\Delta H (H - H_{res})}{[(H - H_{res})^2 + \Delta H^2]}, \quad (1)$$

where V_S, V_A, ΔH, and H_{res} are the symmetric and antisymmetric Lorentzian components, the linewidth, and the resonance field, respectively. Based on the generated spin current with conventional spin-polarization σ_y via SHE/iREE, V_S is proportional to the out-of-plane DL torque effective field H_{DL}, while V_A is related to the sum of the in-plane Oersted field H_{Oe} and in-plane FL torque effective field H_{FL}.

To investigate the interface-related SOTs, we measured the ST-FMR spectra with various Py layer thicknesses (t) for the Pt/ML/Py trilayers. Figures 2(a)–2(d) show the representative ST-FMR spectra V_{mix} for Pt/Py, Pt/Co/Py, Pt/Fe/Py, and Pt/Ni/Py at $f = 9$ GHz and $\varphi = 30^\circ$. The ratio of the magnitude of the symmetric and antisymmetric Lorentzian components (V_S/V_A) is extracted by fitting V_{mix} spectra using

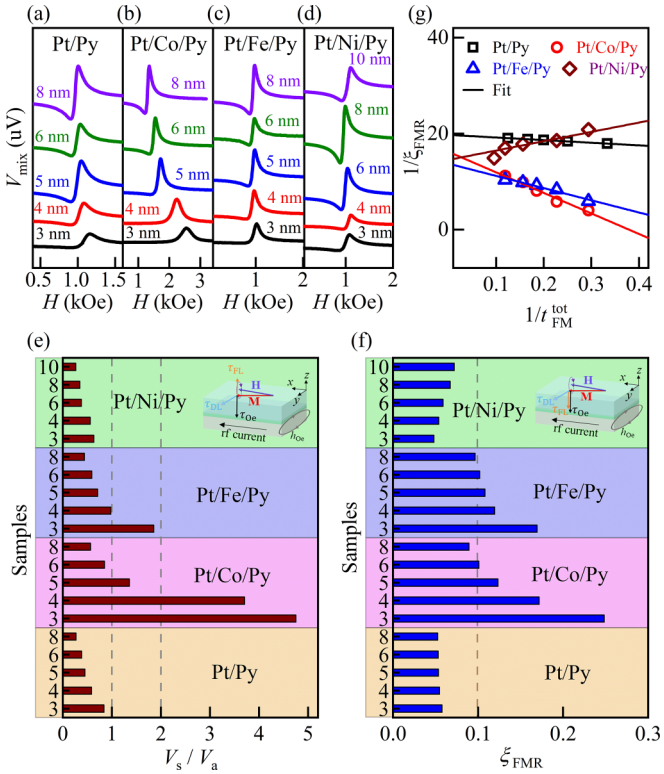

FIG. 2. (a)–(d) The representative ST-FMR spectra of Pt/Py(t) (a), Pt/Co/Py(t) (b), Pt/Fe/Py(t) (c), and Pt/Ni/Py(t) (d) at $f = 9$ GHz and $\varphi = 30°$. The Py thickness t is labeled in the panel. (e), (f) The ratio of V_S/V_A (e) and FMR-SOT efficiencies ξ_{FMR} (f) for five different series of samples with various Py thicknesses. The insets illustrate the SOTs and Oersted field torque in the opposite (e) and same (f) directions to the FL torque. (g) The inverse of SOT efficiency ($1/\xi_{FMR}$) as a function of the inverse of the total magnetic layer thickness ($1/t_{FM}^{tot}$) for all Pt-based devices. The symbols and solid lines are the experimental data and the linear fitting results, respectively.

Eq. (1). The FMR spin-torque generation efficiency ξ_{FMR} is determined by the ratio of V_S/V_A as follows [40–42]:

$$\xi_{FMR} = \frac{V_S}{V_A}\frac{e\mu_0 M_s t_{FM}^{tot} t_{HM}}{\hbar}\sqrt{1 + 4\pi M_{eff}/H_{res}}\,, \qquad (2)$$

where t_{HM}, t_{FM}^{tot}, e, and $\hbar$ represent the thickness of the HM layer and the total FM layer, the electronic charge, and reduced Planck's constant, respectively. The effective demagnetization $4\pi M_{eff}$ is obtained by fitting the experimental dispersion of f vs H_{res} using the Kittel formula [7,41]: $f = (\gamma/2\pi)\sqrt{H_{res}(H_{res} + 4\pi M_{eff})}$, where $\gamma/2\pi$ is the gyromagnetic ratio.

Figures 2(e) and 2(f) show the obtained V_S/V_A and ξ_{FMR} for all Pt/ML/Py samples with different Py layer thicknesses. For all these Pt-based samples, the sign of V_S and V_A is positive and stays unchanged for all studied Py layer thicknesses, consistent with the positive spin Hall angle of Pt [18,27] and the dominant Oersted field torque against FL torque ($V_A \propto \tau_{Oe} - \tau_{FL}$) [inset of Fig. 2(e)] [43,44], or a superposition of the Oersted field and FL torques ($V_A \propto \tau_{Oe} + \tau_{FL}$) [inset of Fig. 2(f)]. Compared to the Pt/Py without inserting layer, the ratio of V_S/V_A exhibits a significant enhancement for the inserting Co and Fe, but suppression for the inserting Ni. As shown in Fig. 2(f), the ξ_{FMR} can also be substantially tuned by inserting ultrathin ML metals. The ST-FMR efficiency ξ_{FMR} is related to DL- and FL-SOT efficiencies [41]: $\xi_{DL(FL)} = (2e/\hbar)\mu_0 M_s t_{FM}^{tot} H_{DL(FL)}/j_c$, where j_c represents the rf current density in the HM layer. ξ_{FMR} depends on t_{FM}^{tot} because H_{FL} is inversely proportional to the total FM layer thickness in terms of $H_{FL} \propto \xi_{FL}/t_{FM}^{tot}$, and H_{Oe} is independent of t_{FM}^{tot} if j_c in the HM layer stays the same [41,42]:

$$\frac{1}{\xi_{FMR}} = \frac{1}{\xi_{DL}}\left(1 + \frac{\hbar}{e}\frac{\xi_{FL}}{\mu_0 M_s t_{FM}^{tot} t_{HM}}\right). \qquad (3)$$

To determine the DL torque and FL torque efficiencies (ξ_{DL} and ξ_{FL}), we plot the $1/\xi_{FMR}$ as a function of $1/t_{FM}^{tot}$ for all Pt-based samples in Fig. 2(g). Figure 2(g) shows that the sign of the intercept of all linear relations is positive, indicating that $\xi_{DL} > 0$ for all Pt-based samples, consistent with the positive spin Hall angle of Pt. In addition, the Pt/Co, Fe, and Ni/Py samples show a smaller intercept value than the Pt/Py bilayer, indicating that the ultrathin ML (Co, Fe, Ni) insertion can significantly enhance ξ_{DL}.

Furthermore, Fig. 2(g) shows that the Pt/Ni/Py exhibits a positive slope that is opposite to the other four Pt-based systems, indicating that the sign of ξ_{FL} is reversed by inserting an ultrathin Ni layer. We note that according to the linear dependence of $1/\xi_{FMR}$ on $1/t_{FM}^{tot}$ and Eq. (3), one can exclude the additional contributions, including the spin-pumping and thermal effects for ξ_{DL} and ξ_{FL}. The determined values of ξ_{DL} and ξ_{FL} for all five series samples from Fig. 2(g) are summarized in Table I.

B. Interfacial spin-transport parameters in Pt-based trilayers

According to the SOT-generation mechanism, the interface-generated spin currents and the interfacial spin transmission T_{int} can significantly contribute to SOT efficiency besides the bulk SHE inside the Pt layer. To shed light on how the inserting ultrathin ML spacer impacts the DL and FL torque efficiencies, we further characterize the interfacial properties of the Pt/ML/Py trilayers by quantifying the interfacial magnetic anisotropy energy density K_s, the real and imaginary part of the effective spin-mixing conductance $\mathrm{Re}(G_{eff}^{\uparrow\downarrow})$ and $\mathrm{Im}(G_{eff}^{\uparrow\downarrow})$, respectively, and the two-magnon scattering coefficient (β_{TMS}). First, the K_s can be quantified from the $1/t_{FM}^{tot}$ dependence of $4\pi M_{eff}$ using the following formula [40,41]:

$$4\pi M_{eff} = 4\pi M_s - \frac{2K_s}{\mu_0 M_s}\frac{1}{t_{FM}^{tot}}. \qquad (4)$$

We determined $4\pi M_{eff}$ by fitting the measured f vs H_{res} using the Kittel formula, as shown in the representative Pt/Co/Py samples in Fig. 3(a). Since the ML insertion layers are strongly exchange coupled to the adjacent Py layer, the magnetic layer ML/Py is considered as a single magnetic unit. For instance, the total saturation magnetization M_s of the ML/Py is determined by the formula of $M_s = (M_s^{Py} t_{Py} + M_s^{ML} t_{ML})/(t_{Py} + t_{ML})$, where the M_s^{Py} and M_s^{ML} are the saturation magnetization of Py and

TABLE I. The parameters of the DL torque efficiency ξ_{DL}, the FL torque efficiency ξ_{FL}, the interfacial PMA energy density K_s, two-magnon scattering coefficient β_{TMS}, the real and imaginary part of the total effective spin-mixing conductance $\mathrm{Re}(G_{eff}^{\uparrow\downarrow})$ and $\mathrm{Im}(G_{eff}^{\uparrow\downarrow})$, and the intrinsic magnetic damping constant α_{int} for the Pt/Py, Pt/Co/Py, Pt/Fe/Py, Pt/Gd/Py, Pt/Ni/Py, and Ta/Ni/Py systems.

Sample	ξ_{DL}	ξ_{FL}	K_s(erg/cm^2)	β_{TMS}(nm^2)	$\mathrm{Re}(G_{eff}^{\uparrow\downarrow})(10^{15}\Omega^{-1}\,\mathrm{m}^{-2})$	$\mathrm{Im}(G_{eff}^{\uparrow\downarrow})(10^{15}\Omega^{-1}\,\mathrm{m}^{-2})$	α_{int}
Pt/Py	0.051	−0.002	0.255	0.124	0.500	−1.461	0.010
Pt/Co/Py	0.062	−0.023	1.402	0.211	0.747	0.455	0.014
Pt/Fe/Py	0.073	−0.016	0.078	0.082	0.482	−0.340	0.010
Pt/Ni/Py	0.068	0.011	0.242	0.157	0.675	−0.096	0.008
Ta/Ni/Py	−0.108	−0.034	0.060	0.052	−0.223	−1.194	0.008

ML, respectively. For the representative 6-nm-thickness samples, $M_s^{Py} = 716\,\mathrm{emu/cm^3}$, $M_s^{Co} = 1130\,\mathrm{emu/cm^3}$, $M_s^{Fe} = 1440\,\mathrm{emu/cm^3}$, and $M_s^{Ni} = 382\,\mathrm{emu/cm^3}$ are measured by vibrating sample magnetometry, consistent with previously reported values [5,40,41]. The obtained K_s by fitting the experimental results using Eq. (4) in Fig. 3(b) is summarized in Table I. K_s of Pt/Co/Py is several times larger than that of Pt/Py, which is related to the strong interfacial perpendicular magnetic anisotropy (PMA) for Pt/Co due to the strong iSOC. However, for the Ni and Fe inserting layers, they have a small K_s comparable to the Pt/Py sample.

Furthermore, the $\mathrm{Re}(G_{eff}^{\uparrow\downarrow})$ and interfacial β_{TMS} can also be characterized by analyzing the thickness-dependent magnetic damping. Figure 3(c) shows the linewidth ΔH of the ST-FMR spectra as a function for the representative Pt/Co/Py(t) samples. The effective Gilbert damping α_{eff} can be determined by fitting these experimentally obtained linewidth ΔH data using the formula of $\Delta H = (2\pi/\gamma)\alpha_{eff} f + \Delta H_0$, where ΔH_0 is the inhomogeneous linewidth. The effective Gilbert damping α_{eff} is further expressed as [45,46]

$$\alpha_{eff} = \alpha_{int} + \mathrm{Re}(G_{eff}^{\uparrow\downarrow})\frac{g\mu_B h}{4\pi M_s e^2}\frac{1}{t_{FM}^{tot}} + \beta_{TMS}\frac{1}{t_{FM}^{tot\,2}}, \quad (5)$$

where g is the Landé factor, μ_B is the Bohr magnetron, and h is Planck's constant. The first term is the total magnetic layer thickness-independent intrinsic Gilbert damping α_{int}, the second term is related to the spin-current loss via spin pumping into the Pt layer and being absorbed due to spin memory

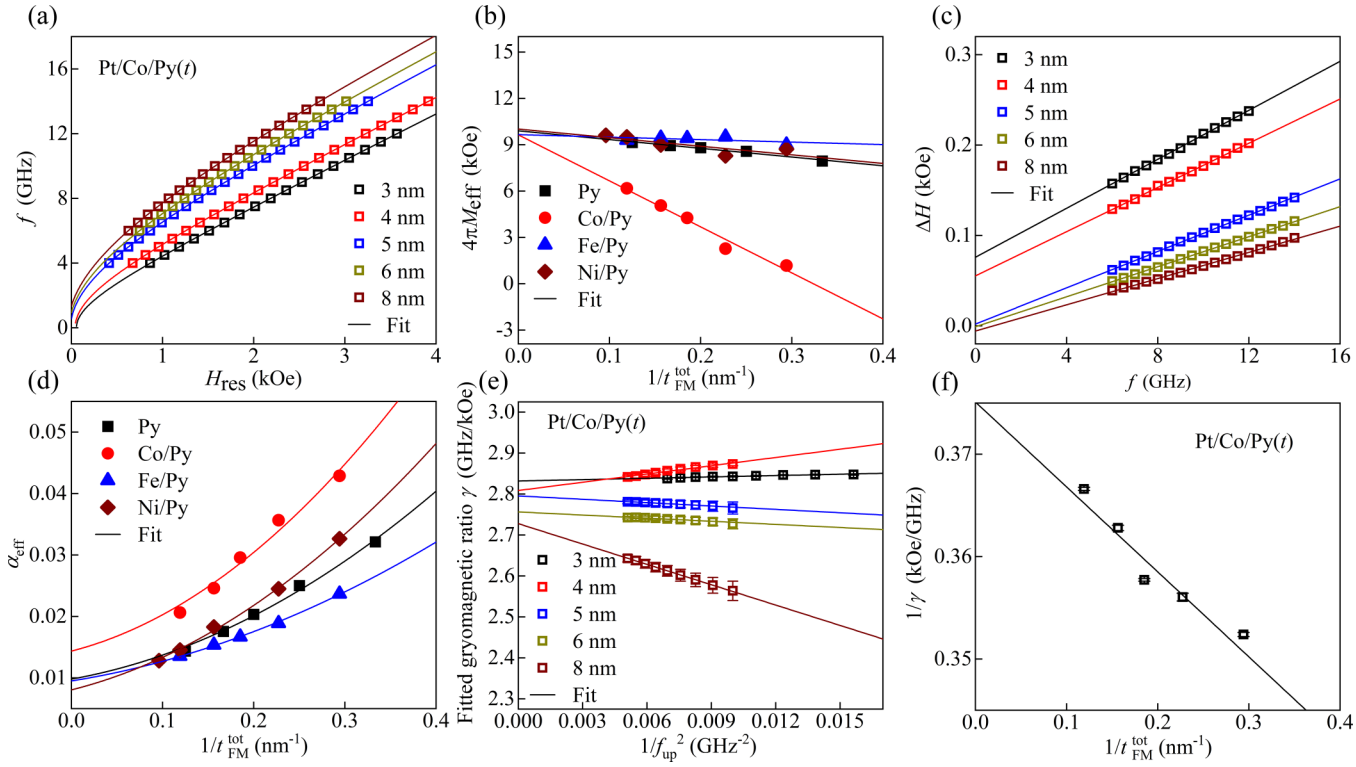

FIG. 3. (a) The dispersion relation curves between f and H_{res} (symbols) and the corresponding Kittel fittings (solid curves) for the Pt/Co/Py(t) samples. (b) The effective demagnetization field $4\pi M_{eff}$ as a function of $1/t_{FM}^{tot}$ for all five series of Pt/ML/Py(t) samples. The solid lines are the linear-fitting result. (c) Linewidth ΔH vs resonance frequency f. The solid lines are the linear fitting. (d) Damping α_{eff} as a function of $1/t_{FM}^{tot}$ (symbols). The lines are the fitting results using Eq. (5). (e) The fitted value of the gyromagnetic ratio γ_{fit} as a function of $1/f_{up}^2$ for Pt/Co/Py(t) samples. The lower fitting frequencies are fixed at 4 GHz and the error bars are also plotted. The solid lines are the linear fitting. (f) The inverse gyromagnetic ratio $1/\gamma$ as a function of the inverse FM thickness $1/t_{FM}^{tot}$. The solid line is the linear fitting.

loss at the Pt–ML and ML–Py interfaces, and the third term is the contribution from the TMS process. The interface β_{TMS} depends on $(2K_s/M_s)^2$ and/or the density of magnetic defect at the interfaces. To determine the $\mathrm{Re}(G_{\mathrm{eff}}^{\uparrow\downarrow})$ and interface β_{TMS}, we plot the obtained α_{eff} as a function of $1/t_{\mathrm{FM}}^{\mathrm{tot}}$ in Fig. 3(d). The values extracted by fitting $1/t_{\mathrm{FM}}^{\mathrm{tot}}$ dependence of α_{eff} using Eq. (5) are summarized in Table I. Consistent with the large K_S above, the intrinsic Gilbert damping for the Pt/Co/Py sample is more than 1.4 times that of the other four series. Meanwhile, the Pt/Co/Py has a larger ST-FMR linewidth obtained at $f = 6$ GHz than other systems with $t = 6$ nm.

Additionally, in FM/NM systems, the gyromagnetic ratio γ is also modified by the spin current pumped by FMR [47,48]:

$$\frac{1}{\gamma} = \frac{1}{\gamma_0}\left\{1 - \mathrm{Im}(G_{\mathrm{eff}}^{\uparrow\downarrow})\frac{g\mu_{\mathrm{B}}\mathrm{h}}{4\pi M_s e^2}\frac{1}{t_{\mathrm{FM}}^{\mathrm{tot}}}\right\}, \tag{6}$$

where γ_0 represents the intrinsic gyromagnetic ratio of the isolated FM. Thus, we can calculate the imaginary part by the linear fitting of the inverse gyromagnetic ratio on the inverse FM thickness. Prerequisitely, we have to determine the gyromagnetic ratio of samples with different FM thicknesses. Here, we follow the methodology presented in Ref. [49] and adopt an asymptotic analysis to the data obtained over a finite range of frequencies. The fitted value γ_{fit} has a strong dependence on the range of the fitting frequency. With an identical lower bound on the data used in the fitting, the precise determination of γ is the asymptotic value as the upper fitting frequency $f_{\mathrm{up}} \to \infty$. Empirically, the γ_{fit} is linearly proportional to $1/f_{\mathrm{up}}^2$ and thus, the precise γ is determined by the intercept of the linear fitting. Finally, we can obtain the imaginary part of the spin-mixing conductance from the slope of the linear fitting of $1/\gamma$ on $1/t_{\mathrm{FM}}^2$. The calculation results of Pt/Co/Py(t) are shown in Figs. 3(e) and 3(f), and the other results are also summarized in Table I.

From the DL and FL torque efficiencies and the interface-dependent spin-transport parameters in Table I, we deduce that the enhanced SOT efficiency with Co insertion are the result of competition between the enhancement of iREE-generated SOTs and β_{TMS}. Both of these are closely related to the strong iSOC at the Pt/Co interface. For the Fe insertion, the smaller β_{TMS} and negligible K_s indicate that the Pt/Fe interface can improve the interfacial spin transparency and/or the interfacial spin accumulation via enhancing the exchange interaction for more considerable SOTs efficiencies.

In the Pt/Ni/Py configuration, the enhancement of ξ_{DL} may be linked to the improvement of the interfacial spin transparency and the additional interface-generated spin currents, e.g., orbital current and orbital-to-spin conversion in the Pt/Ni and Ni sublayer [50,51]. In contrast, the positive ξ_{FL} is opposite to the other four Pt-based systems. Unlike the DL torque related to the absorption of spin current, the FL torque arises from the reflection of the spin current at the HM–FM interfaces. Therefore, the FL torque is more sensitive to changes in the interfacial electronic structure when different ML spacers are inserted. According to previously reported sign reversal of SOTs due to the orbital torque in the Nb/Ni, Ta/Ni, and Cr/Ni bilayers [50–52], in our case the sign reversal of ξ_{FL} observed in the ultrathin Ni insertion system would also be correlated to the secondary spin currents due to orbital-to-spin conversion

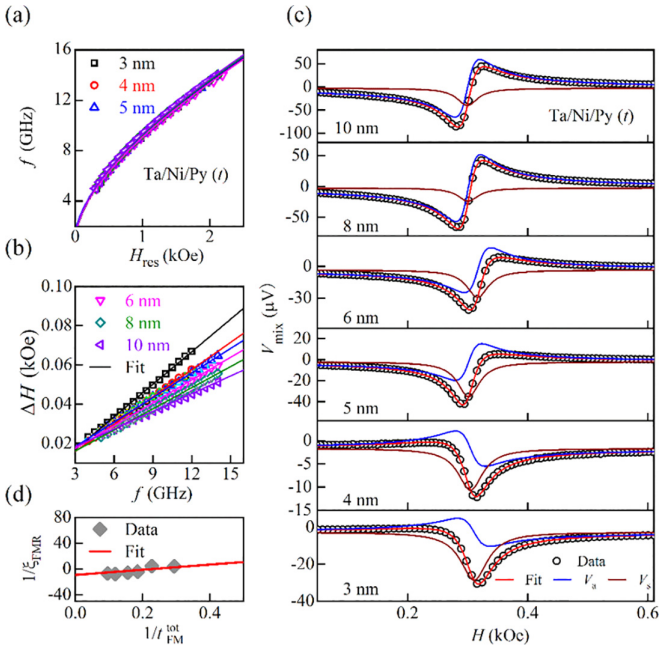

FIG. 4. (a) The experimental dispersion curves of f vs H_{res} (symbols) and the corresponding Kittel fittings (solid curves) for a series of Ta(6)/Ni(0.4)/Py(t) samples with the labeled Py thickness t. (b) Linewidth ΔH vs resonance frequency f. The solid lines are the linear fittings. (c) The typical ST-FMR spectra V_{mix} obtained at $f = 5$ GHz and the corresponding Lorentzian fitting curves using Eq. (1). (d) The experimental data of $1/\xi_{\mathrm{FMR}}$ vs $1/t_{\mathrm{FM}}^{\mathrm{tot}}$, and their linear fitting using Eq. (5). The error bars are significantly smaller than the data symbols.

occurring at the Pt/Ni interface or inside the Ni spacer, since Ni possesses the largest orbital-to-spin conversion efficiency compared with the other ML according to the first-principle calculated results [50].

C. Spin-orbit torques in Ta/Ni/Py trilayers

To further investigate the sign reversal of fieldlike torque caused by inserting an ultrathin Ni spacer in the Pt/Py system, we adopt the Ta(6)/Ni(0.4)/Py(t) system as a control experiment. Figure 4(a) shows that the corresponding six dispersion curves of a series of Ta/Ni/Py(t) with t = 3-, 4-, 5-, 6-, 8-, and 10-nm samples collapse into a single curve, which the Kittel formula can fit well with nearly the same parameter, $M_{\mathrm{eff}} = 780\,\mathrm{emu/cm^3}$, suggesting a good consistency for the series of samples and a weak interfacial perpendicular magnetic anisotropy (PMA) energy density K_s at the Ta/Ni interface. The effective Gilbert damping α_{eff} can be determined by linearly fitting the linewidth ΔH vs f data in Fig. 4(b). Furthermore, α_{int}, β_{TMS}, $\mathrm{Re}(G_{\mathrm{eff}}^{\uparrow\downarrow})$, and $\mathrm{Im}(G_{\mathrm{eff}}^{\uparrow\downarrow})$ can be extracted by fitting $1/t_{\mathrm{FM}}^{\mathrm{tot}}$ dependence of α_{eff} and $1/\gamma$ using Eqs. (5) and (6), respectively, the same as in Figs. 3(d) and 3(f). These values for Ta/Ni/Py trilayer system are also summarized in Table I.

Figure 4(c) shows the representative ST-FMR spectra obtained at $f = 5$ GHz and their Lorentzian fitting curves with Eq. (1). The blue and brown lines represent the antisymmetric V_{A} and symmetric components V_{S} of the V_{mix} spectra,

respectively. In contrast to the Pt/Ni/Py system, the V_S signal reflecting the DL torque is negative and opposite to the Pt-based system in Fig. 2(e), consistent with the expectation because of the negative spin Hall angle for Ta. The negative intercept $\xi_{DL} = -0.108$ of the linear fitting $1/\xi_{FMR}$ vs $1/t_{FM}^{tot}$ using Eq. (3), as shown in Fig. 4(d), also confirms it. More surprisingly, we find the V_A signal reversal during increasing Py thickness from $t \leqslant 4$ to $t \geqslant 5$ nm. Based on the discussion of Pt-based systems above, the Oersted field torque τ_{Oe} has the dominant contribution to V_A for all studied samples with different Py thicknesses because Pt has a higher conductance than the studied ML. However, for Ta/Ni/Py system, the Oersted field H_{Oe} is expected to be reduced significantly if the total rf input current stays the same for Pt- and Ta-based systems because Ta has more than 10 times lower conductance than Pt. In addition, the FL torque is inversely proportional to the thickness of the FM layer $H_{FL} = \frac{\hbar}{2e}\frac{\xi_{FL}J_{rf}}{4\pi M_s t_{FM}}$, and thus decreases with increasing Py thickness, while the current-induced Oersted field on the FM layer $H_{Oe} = \frac{J_{rf}t_{NM}}{2}$ is approximately linearly proportional to the thickness of the underlying NM layer and remains identical in the series with a constant thickness of the Ta layer [41]. Therefore, the V_A signal reversal with t_{FM} infers that the considerable FL torque τ_{FL} and τ_{Oe} have the opposite direction in the Ta/Ni/Py system [43,44], as illustrated in the inset of Fig. 2(f).

Next, from the linear fitting $1/\xi_{FMR}$ vs $1/t_{FM}^{tot}$ using Eq. (3), we obtain the torque efficiencies $\xi_{DL} = -0.108$ and $\xi_{FL} = -0.034$ for Ta(6)/Ni(0.4)/Py(t) system. Contrary to the Pt/Ni/Py discussed above, both DL and FL torques in Ta/Ni/Py have the same sign as the pure Ta/Py. However, the previously reported Ta/Ni and Nb/Ni exhibit the positive sign for both DL and FL torques, opposite to Ta(6)/Ni(0.4)/Py(t), Ta/Py, and Nb/Py [51]. The reported sign reversal of DL and FL torques in Ta/Ni and Nb/Ni bilayers indicates that a strong orbital current is generated in Ta and Nb sublayers and then converted into the spin currents inside the Ni sublayer [52]. Furthermore, previous studies report that the orbital-to-spin conversion length is generally several nanometers [53,54]. Therefore, in our case, the 0.4-nm-thick Ni insertion layer is too thin to convert the input orbital current to spin current completely and sufficiently. Thus, the sign of ξ_{FL} in Ta/Ni/Py remains unchanged. Additionally, the enhancement (suppression) of ξ_{DL} in Pt/Ni/Py (Ta/Ni/Py) is also consistent with the expected positive sign of orbital torque in Pt- and Ta-based systems because, unlike spin Hall conductivity, the orbital Hall conductivity is positive for both Pt and Ta [55].

D. Discussion of sign reversal of ξ_{FL} in Pt/Ni bilayer and Pt/Ni/Py trilayer

There have been some preceding studies on the ξ_{FL} in various systems, mainly focusing on the influence of interfacial effects. For example, in the Pt/Ni and Pt/Fe bilayer systems, the ξ_{DL} is almost identical, while the ξ_{FL} exhibits opposite signs despite the same underlying Pt sublayer [40]. In Ref. [40], this is attributed to the sign change of the imaginary part of the spin-mixing conductance resulting from different interfacial electronic structures. We also plot all the calculated results of both ξ_{DL}, $\mathrm{Re}(G_{eff}^{\uparrow\downarrow})$ and ξ_{FL}, $\mathrm{Im}(G_{eff}^{\uparrow\downarrow})$ of all studied samples in Fig. 5. According to the previous theories based on the drift-diffusion approximation [16,17,41], in the absence of spin memory loss, the torque efficiencies have a relation with the spin-mixing conductance as

$$\xi_{DL} = \theta_{SH}\mathrm{Re}\left\{\frac{2G_{eff}^{\uparrow\downarrow}\tanh\left(\frac{d_{NM}}{\lambda_{s,NM}}\right)}{G_{NM}\coth\left(\frac{d_{NM}}{\lambda_{s,NM}}\right)}\right\},$$
$$\xi_{FL} = \theta_{SH}\mathrm{Im}\left\{\frac{2G_{eff}^{\uparrow\downarrow}\tanh\left(\frac{d_{NM}}{\lambda_{s,NM}}\right)}{G_{NM}\coth\left(\frac{d_{NM}}{\lambda_{s,NM}}\right)}\right\}, \quad (7)$$

where $G_{NM} \equiv \sigma_{NM}/\lambda_{s,NM}$ is the spin conductance of the NM. Even considering the potential strong spin scattering and spin memory loss induced by the ultrathin FM insertion layers, the torque efficiencies should retain a general proportionality to the spin-mixing conductance. As depicted in Fig. 5(a), the $\mathrm{Re}(G_{eff}^{\uparrow\downarrow})$ can roughly interpret the ξ_{DL} variation induced by ultrathin FM insertion layer. However, the $\mathrm{Im}(G_{eff}^{\uparrow\downarrow})$ fails to reproduce the changes in ξ_{FL}, either the rise-and-fall trends or the positive-negative sign characteristics. Such a discrepancy highlights the possibility that our experimental results might go beyond the conventional interpretation, which primarily takes into account the spin degree, including either the SHE in bulk NM or interface-generated spin currents, but neglects the orbital degree.

As for the Ta/Ni and Nb/Ni bilayers mentioned above [50,51], both ξ_{DL} and ξ_{FL} reverse their signs compared to Ta/Py and Nb/Py, as summarized in Table II. The widely recognized reason is that the Ta/Ni and Nb/Ni systems generate considerable orbital current-converted spin currents with the polarization opposite to the SHE-generated spin currents because of a high orbital-to-spin conversion efficiency in the Ni sublayer and a positive giant orbital Hall (OH) conductivity σ_{OH} in the Ta and Nb sublayers [50,51], which differs from both positive signs for spin Hall and orbital Hall conductivities in the Pt. In our studied Ta/Ni/Py trilayer with a 0.4-nm-thick Ni spacer, the values of both ξ_{DL} and ξ_{FL} are reduced significantly compared to the Ta/Py bilayer, but their signs remain unchanged. The reason is that the ultrathin Ni spacer is thinner than the orbital-to-spin conversion length of several nanometers [53,54], so the orbital currents generated by the Ta sublayer are not fully converted into spin currents in only 0.4-nm-thick Ni spacer and cannot wholly surpass the SHE-generated spin currents with the negative sign and reverse the sign of ξ_{DL} and ξ_{FL} as the previously reported Ta/Ni bilayer [50]. Different from Ta/Ni/Py trilayer, our studied Pt/Ni/Py system exhibits a sign change of the ξ_{FL}, the same as the previous Pt/Ni bilayer.

However, according to Hund's rules and first-principle calculated results [50], Fe, Co, and Ni all exhibit positive orbital-to-spin conversion efficiency, indicating that the spin current converted from orbital currents by the Ni sublayer shares the same polarization with the SHE-generated spin currents within the Pt sublayer. Thus, it might be insufficient to account for the observed sign reversal of ξ_{FL} within the previously reported Pt/Ni bilayer and our Pt/Ni/Py trilayer if only considering the signs of the spin Hall and OH conductivities of the Pt sublayer and the orbital-to-spin conversion

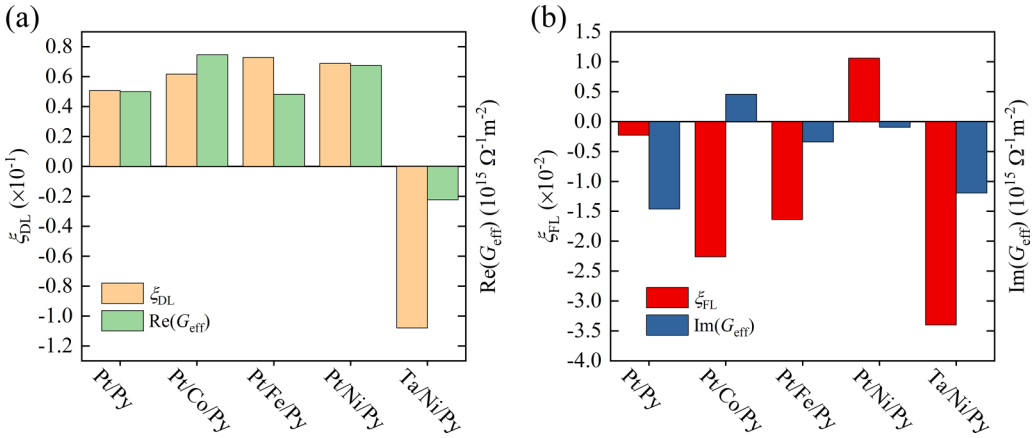

FIG. 5. Calculated results of (a) dampinglike torque efficiency ξ_{DL} and the real part of the effective spin-mixing conductance $\mathrm{Re}(G_{eff}^{\uparrow\downarrow})$, and (b) fieldlike torque efficiency ξ_{FL} and the imaginary part of the effective spin-mixing conductance $\mathrm{Im}(G_{eff}^{\uparrow\downarrow})$, respectively.

of the Ni sublayer, as summarized in Table III. Based on all sign results of ξ_{DL} and ξ_{FL} for various systems in Table II, we propose a possible reason for the sign reversal of ξ_{FL} and the enhancement of ξ_{DL} in Pt/Ni/Py. This explanation considers the influence of orbital-to-spin conversion occurring within the Ni insertion layer or at the Pt/Ni interface, thereby contributing to ξ_{FL} with a polarization opposite to that of SHE-generated spin currents within the Pt sublayer or other potentially underestimated origins impacting the FL torque. Different from the prominent ξ_{FL} in Ta-based systems, Pt-based systems exhibit a significantly smaller ξ_{FL} than ξ_{DL} so that the emergence of secondary abnormal attributions to the FL torque can be easily observed. Our experimentally observed abnormal sign reversal of the FL torque in the Pt/Ni/Py system warrants further theoretical and modeling studies of spin Hall, orbital Hall effects, the conversion between them, and the relationship between them and spin torques in the most-studied NM–FM bilayer systems.

Apart from the orbital torque mechanism, we also analyze other possible interface-related spin-dependent scattering mechanisms, particularly the spin-filtering effect [56]. The spin-filtering effect originates from the interfacial momentum-dependent spin-orbit field, such as the Rashba or Dresselhaus effective fields [12,13]. The electrons with spins parallel or antiparallel to these interfacial spin-orbit fields experience different scattering amplitudes. Consequently, the reflected and transmitted electrons become spin polarized even if the incoming electrons are unpolarized. However, this scenario diverges from our experimental configuration, where the spin Hall effect in the underlying Pt layer generates the spin currents with a transverse spin polarization. These spin-polarized currents might substantially encounter distinct scattering amplitudes when passing through the Pt–ML and ML–Py interfaces, resulting in different spin transparencies, which have already been partly characterized through the spin-mixing conductance above. It is also important to note that even if the spin-filtering effect or interface-generated spin currents play an important role [16], the generated spin currents would naturally diffuse and flow into the adjacent FM layer and modulate both the dampinglike and fieldlike torque efficiencies. Also note that the interfaces between Pt and Fe, Co, Ni exhibit inversion symmetry breaking and the same heavy-metal Pt sublayer. These attributes give rise to the Rashba effective field with the same orientation due to the expected surface-potential gradient with the same direction, implying that subsequent modifications in torque efficiencies have the same tendency across these interfaces [16,17,57]. This perspective, however, is inconsistent with our experimental results that only the fieldlike torque efficiency exhibits a sign change with Ni insertion alone.

IV. CONCLUSION

In summary, our study examines the SOT efficiencies in the HM–ML–Py trilayers with 0.4-nm-thick Co, Fe, and Ni spacer, employing the ST-FMR spectra technique. Compared to the Pt/Py bilayer with $\xi_{DL} \sim 0.051$, we find that the DL torque efficiency ξ_{DL} is significantly enhanced by inserting an ultrathin ML spacer to modulate the interfacial spin transparency and/or the interface-generated spin currents, including iREE and orbital-to-spin conversion. Besides the DL torque, the FL torque is significantly enhanced for all ML inserting systems and even changes its sign in the Ni insertion system. In contrast with Pt/Ni/Py system, Ta/Ni/Py system demonstrates a notable reduction in ξ_{DL}, but does not

TABLE II. Signs of the dampinglike torque efficiency ξ_{DL} and the fieldlike torque efficiency ξ_{FL} in selected systems.

	Pt/Fe	Pt/Fe(0.4)/Py	Pt/Ni	Pt/Ni(0.4)/Py	Ta/Py	Ta/Ni	Ta/Ni(0.4)/Py	Nb/Py	Nb/Ni
ξ_{DL}	+	+	+	+	−	+	−	−	+
ξ_{FL}	−	−	+	+	−	+	−	−	+
Refs.	[40]	This paper	[40]	This paper	[51,52]	[51,52]	This paper	[52]	[52]

TABLE III. Signs of orbital-to-spin conversion efficiency (spin-orbit coupling) $\langle \boldsymbol{L} \cdot \boldsymbol{S} \rangle$, spin Hall conductivity σ_{SH}, and orbital Hall conductivity σ_{OH} of selected elements.

	Fe	Co	Ni	Pt	Ta	Nb
$\langle \boldsymbol{L} \cdot \boldsymbol{S} \rangle$	+	+	+	+		
σ_{SH}	+	+	+	+	−	−
σ_{OH}			+	+	+	+
Refs.	[51]	[45]	[45]	[51]	[51,52]	[52]

change the sign of SOTs by inserting a 0.4-nm-thick Ni spacer. The specific results for the ultrathin Ni insertion systems may find explanation in the secondary spin currents due to the OHE-generated orbital currents in the NM, subsequently converted to spin currents in the Ni insertion layer and/or Pt/Ni and Ta/Ni interfaces. Further theories and numerous models are essential to clarify these various spin-current generation mechanisms, especially for orbital-to-spin current conversion and spin-polarization directions in the FM and its interface, which would facilitate the electrical control of perpendicular nanomagnets for SOT-MRAM with promising high performance.

ACKNOWLEDGMENTS

The project is supported by the National Key Research and Development Program of China (Grant No. 2023YFA1406603), National Natural Science Foundation of China (Grant No. 12074178), the Open Research Fund of Jiangsu Provincial Key Laboratory for Nanotechnology, and the Key Research and Development Program of Zhejiang Province under Grant No. 2021C01039.

[1] L. Q. Liu, T. Moriyama, D. C. Ralph, and R. A. Buhrman, Spin-torque ferromagnetic resonance induced by the spin Hall effect, Phys. Rev. Lett. **106**, 036601 (2011).

[2] L. Q. Liu, C. F. Pai, Y. Li, H. W. Tseng, D. C. Ralph, and R. A. Buhrman, Spin-torque switching with the giant spin Hall effect of tantalum, Science **336**, 555 (2012).

[3] Q. Fu, L. Liang, W. Wang, L. Yang, K. Zhou, Z. Li, C. Yan, L. Li, H. Li, and R. Liu, Observation of nontrivial spin-orbit torque in single-layer ferromagnetic metals, Phys. Rev. B **105**, 224417 (2022).

[4] L. Yang, Y. Gu, L. Chen, K. Zhou, Q. Fu, W. Wang, L. Li, C. Yan, H. Li, L. Liang, Z. Li, Y. Pu, Y. Du, and R. Liu, Absence of spin transport in amorphous YIG evidenced by nonlocal spin transport experiments, Phys. Rev. B **104**, 144415 (2021).

[5] L. Yang, Y. Fei, K. Zhou, L. Chen, Q. Fu, L. Li, C. Yan, H. Li, Y. Du, and R. Liu, Maximizing spin–orbit torque efficiency of Ta(O)/Py via modulating oxygen-induced interface orbital hybridization, Appl. Phys. Lett. **118**, 032405 (2021).

[6] L. Li, L. Chen, R. Liu, and Y. Du, Recent progress on excitation and manipulation of spin-waves in spin Hall nano-oscillators, Chin. Phys. B **29**, 117102 (2020).

[7] W. Wang, Q. Fu, K. Zhou, L. Chen, L. Yang, Z. Li, Z. Tao, C. Yan, L. Liang, X. Zhan, Y. Du, and R. Liu, Unconventional spin currents generated by the spin-orbit precession effect in perpendicularly magnetized Co-Tb ferrimagnetic system, Phys. Rev. Appl. **17**, 034026 (2022).

[8] M. Wang, W. Cai, D. Zhu, Z. Wang, J. Kan, Z. Zhao, K. Cao, Z. Wang, Y. Zhang, T. Zhang, C. Park, J.-P. Wang, A. Fert, and W. Zhao, Field-free switching of a perpendicular magnetic tunnel junction through the interplay of spin-orbit and spin-transfer torques, Nat. Electron. **1**, 582 (2018).

[9] I. M. Miron, K. Garello, G. Gaudin, P. J. Zermatten, M. V. Costache, S. Auffret, S. Bandiera, B. Rodmacq, A. Schuhl, and P. Gambardella, Perpendicular switching of a single ferromagnetic layer induced by in-plane current injection, Nature (London) **476**, 189 (2011).

[10] J. Ryu, S. Lee, K. J. Lee, and B. G. Park, Current-induced spin-orbit torques for spintronic applications, Adv. Mater. **32**, 1907148 (2020).

[11] J. E. Hirsch, Spin Hall effect, Phys. Rev. Lett. **83**, 1834 (1999).

[12] I. M. Miron, G. Gaudin, S. Auffret, B. Rodmacq, A. Schuhl, S. Pizzini, J. Vogel, and P. Gambardella, Current-driven spin torque induced by the Rashba effect in a ferromagnetic metal layer, Nat. Mater. **9**, 230 (2010).

[13] J. C. Sanchez, L. Vila, G. Desfonds, S. Gambarelli, J. P. Attane, J. M. De Teresa, C. Magen, and A. Fert, Spin-to-charge conversion using Rashba coupling at the interface between non-magnetic materials, Nat. Commun. **4**, 2944 (2013).

[14] D. Go, D. Jo, C. Kim, and H.-W. Lee, Intrinsic spin and orbital Hall effects from orbital texture, Phys. Rev. Lett. **121**, 086602 (2018).

[15] D. Jo, D. Go, and H.-W. Lee, Gigantic intrinsic orbital Hall effects in weakly spin-orbit coupled metals, Phys. Rev. B **98**, 214405 (2018).

[16] V. P. Amin and M. D. Stiles, Spin transport at interfaces with spin-orbit coupling: Phenomenology, Phys. Rev. B **94**, 104420 (2016).

[17] P. M. Haney, H.-W. Lee, K.-J. Lee, A. Manchon, and M. D. Stiles, Current induced torques and interfacial spin-orbit coupling: Semiclassical modeling, Phys. Rev. B **87**, 174411 (2013).

[18] L. Zhu, D. C. Ralph, and R. A. Buhrman, Maximizing spin-orbit torque generated by the spin Hall effect of Pt, Appl. Phys. Rev. **8**, 031308 (2021).

[19] Q. Shao, P. Li, L. Liu, H. Yang, S. Fukami, A. Razavi, H. Wu, K. Wang, F. Freimuth, Y. Mokrousov, M. D. Stiles, S. Emori, A. Hoffmann, J. Akerman, K. Roy, J.-P. Wang, S.-H. Yang, K. Garello, and W. Zhang, Roadmap of spin-orbit torques, IEEE Trans. Magn. **57**, 800439 (2021).

[20] X. Han, X. Wang, C. Wan, G. Yu, and X. Lv, Spin-orbit torques: Materials, physics, and devices, Appl. Phys. Lett. **118**, 120502 (2021).

[21] Y. Wang, P. Deorani, X. Qiu, J. H. Kwon, and H. Yang, Determination of intrinsic spin Hall angle in Pt, Appl. Phys. Lett. **105**, 152412 (2014).

[22] D. Velázquez Rodriguez, J. E. Gómez, L. Morbidel, P. A. Costanzo Caso, J. Milano, and A. Butera, High spin pumping efficiency in $Fe_{80}Co_{20}$/Ta bilayers, J. Phys. D: Appl. Phys. **54**, 325002 (2021).

[23] P. Yang, Q. Shao, G. Yu, C. He, K. Wong, X. Lu, J. Zhang, B. Liu, H. Meng, L. He, K. L. Wang, and Y. Xu, Enhancement of the spin–orbit torque efficiency in W/Cu/CoFeB heterostructures via interface engineering, Appl. Phys. Lett. **117**, 082409 (2020).

[24] S. K. Li, X. T. Zhao, W. Liu, Y. H. Song, L. Liu, X. G. Zhao, and Z. D. Zhang, Interface effect of ultrathin W layer on spin-orbit torque in Ta/W/CoFeB multilayers, Appl. Phys. Lett. **114**, 082402 (2019).

[25] M. Dc, R. Grassi, J. Y. Chen, M. Jamali, D. Reifsnyder Hickey, D. Zhang, Z. Zhao, H. Li, P. Quarterman, Y. Lv, M. Li, A. Manchon, K. A. Mkhoyan, T. Low, and J. P. Wang, Room-temperature high spin-orbit torque due to quantum confinement in sputtered Bi_xSe_{1-x} films, Nat. Mater. **17**, 800 (2018).

[26] N. H. D. Khang, Y. Ueda, and P. N. Hai, A conductive topological insulator with large spin Hall effect for ultralow power spin-orbit torque switching, Nat. Mater. **17**, 808 (2018).

[27] L. Zhu, D. C. Ralph, and R. A. Buhrman, Highly efficient spin-current generation by the spin Hall effect in $Au_{1-x}Pt_x$, Phys. Rev. Appl. **10**, 031001(R) (2018).

[28] C.-F. Pai, M.-H. Nguyen, C. Belvin, L. H. Vilela-Leão, D. C. Ralph, and R. A. Buhrman, Enhancement of perpendicular magnetic anisotropy and transmission of spin-Hall-effect-induced spin currents by a Hf spacer layer in W/Hf/CoFeB/MgO layer structures, Appl. Phys. Lett. **104**, 082407 (2014).

[29] H. K. Gweon, K.-J. Lee, and S. H. Lim, Spin-orbit torques and their angular dependence in ferromagnet/normal metal heterostructures, Appl. Phys. Lett. **115**, 122405 (2019).

[30] F. Liu, C. Zhou, R. Tang, G. Chai, and C. Jiang, Controllable charge-spin conversion by Rashba-Edelstein effect at Cu/Ta interface, J. Magn. Magn. Mater. **540**, 168462 (2021).

[31] L. Ni, Z. Chen, X. Lu, Y. Yan, L. Jin, J. Zhou, W. Yue, Z. Zhang, L. Zhang, W. Wang, Y.-L. Wang, X. Ruan, W. Liu, L. He, R. Zhang, H. Zhang, B. Liu, R. Liu, H. Meng, and Y. Xu, Strong interface-induced spin-charge conversion in YIG/Cr heterostructures, Appl. Phys. Lett. **117**, 112402 (2020).

[32] Q. Chen, W. Lv, S. Li, W. Lv, J. Cai, Y. Zhu, J. Wang, R. Li, B. Zhang, and Z. Zeng, Spin orbit torques in Pt-based heterostructures with van der Waals interface, Chin. Phys. B **30**, 097506 (2021).

[33] W. L. Peng, J. Y. Zhang, G. N. Feng, X. L. Xu, C. Yang, Y. L. Jia, and G. H. Yu, Enhancement of spin-orbit torque via interfacial hydrogen and oxygen ion manipulation, Appl. Phys. Lett. **115**, 092402 (2019).

[34] H. L. Wang, J. Finley, P. X. Zhang, J. H. Han, J. T. Hou, and L. Q. Liu, Spin-orbit-torque switching mediated by an antiferromagnetic insulator, Phys. Rev. Appl. **11**, 044070 (2019).

[35] C. Y. Guo, C. H. Wan, M. K. Zhao, C. Fang, T. Y. Ma, X. Wang, Z. R. Yan, W. Q. He, Y. W. Xing, J. F. Feng, and X. F. Han, Switching the perpendicular magnetization of a magnetic insulator by magnon transfer torque, Phys. Rev. B **104**, 094412 (2021).

[36] L. Zhu, L. Zhu, and R. A. Buhrman, Fully spin-transparent magnetic interfaces enabled by the insertion of a thin paramagnetic NiO layer, Phys. Rev. Lett. **126**, 107204 (2021).

[37] Q. Li, M. Yang, C. Klewe, P. Shafer, A. T. N'Diaye, D. Hou, T. Y. Wang, N. Gao, E. Saitoh, C. Hwang, R. J. Hicken, J. Li, E. Arenholz, and Z. Q. Qiu, Coherent AC spin current transmission across an antiferromagnetic CoO insulator, Nat. Commun. **10**, 5265 (2019).

[38] X. Shu, J. Zhou, L. Liu, W. Lin, C. Zhou, S. Chen, Q. Xie, L. Ren, Y. Xiaojiang, H. Yang, and J. Chen, Role of interfacial orbital hybridization in spin-orbit-torque generation in Pt-based heterostructures, Phys. Rev. Appl. **14**, 054056 (2020).

[39] W. Zhang, W. Han, X. Jiang, S.-H. Yang, and S. S. P. Parkin, Role of transparency of platinum-ferromagnet interfaces in determining the intrinsic magnitude of the spin Hall effect, Nat. Phys. **11**, 496 (2015).

[40] H. Hayashi, A. Musha, H. Sakimura, and K. Ando, Spin-orbit torques originating from the bulk and interface in Pt-based structures, Phys. Rev. Res. **3**, 013042 (2021).

[41] C.-F. Pai, Y. Ou, L. H. Vilela-Leao, D. C. Ralph, and R. A. Buhrman, Dependence of the efficiency of spin Hall torque on the transparency of Pt/ferromagnetic layer interfaces, Phys. Rev. B **92**, 064426 (2015).

[42] H. Moriya, A. Musha, and K. Ando, Interfacial spin-orbit torque and spin transparency in Co/Pt bilayer, Appl. Phys. Express **14**, 063001 (2021).

[43] T. D. Skinner, M. Wang, A. T. Hindmarch, A. W. Rushforth, A. C. Irvine, D. Heiss, H. Kurebayashi, and A. J. Ferguson, Spin-orbit torque opposing the Oersted torque in ultrathin Co/Pt bilayers, Appl. Phys. Lett. **104**, 062401 (2014).

[44] S. Dutta, A. Bose, A. A. Tulapurkar, R. A. Buhrman, and D. C. Ralph, Interfacial and bulk spin Hall contributions to field-like spin-orbit torque generated by iridium, Phys. Rev. B **103**, 184416 (2021).

[45] L. Zhu, D. C. Ralph, and R. A. Buhrman, Effective spin-mixing conductance of heavy-metal-ferromagnet interfaces, Phys. Rev. Lett. **123**, 057203 (2019).

[46] L. Zhu, L. Zhu, D. C. Ralph, and R. A. Buhrman, Origin of strong two-magnon scattering in heavy-metal/ferromagnet/oxide heterostructures, Phys. Rev. Appl. **13**, 034038 (2020).

[47] M. Zwierzycki, Y. Tserkovnyak, P. J. Kelly, A. Brataas, and G. E. W. Bauer, First-principles study of magnetization relaxation enhancement and spin transfer in thin magnetic films, Phys. Rev. B **71**, 064420 (2005).

[48] G. Tatara and S. Mizukami, Consistent microscopic analysis of spin pumping effects, Phys. Rev. B **96**, 064423 (2017).

[49] J. M. Shaw, H. T. Nembach, T. J. Silva, and C. T. Boone, Precise determination of the spectroscopic g-factor by use of broadband ferromagnetic resonance spectroscopy, J. Appl. Phys. **114**, 243906 (2013).

[50] D. Lee, D. Go, H. J. Park, W. Jeong, H. W. Ko, D. Yun, D. Jo, S. Lee, G. Go, J. H. Oh, K. J. Kim, B. G. Park, B. C. Min, H. C. Koo, H. W. Lee, O. Lee, and K. J. Lee, Orbital torque in magnetic bilayers, Nat. Commun. **12**, 6710 (2021).

[51] S. Dutta and A. A. Tulapurkar, Observation of nonlocal orbital transport and sign reversal of dampinglike torque in Nb/Ni and Ta/Ni bilayers, Phys. Rev. B **106**, 184406 (2022).

[52] S. Lee, M.-G. Kang, D. Go, D. Kim, J.-H. Kang, T. Lee, G.-H. Lee, J. Kang, N. J. Lee, Y. Mokrousov, S. Kim, K.-J. Kim, K.-J. Lee, and B.-G. Park, Efficient conversion of orbital Hall current to spin current for spin-orbit torque switching, Commun. Phys. **4**, 234 (2021).

[53] S. Ding, A. Ross, D. Go, L. Baldrati, Z. Ren, F. Freimuth, S. Becker, F. Kammerbauer, J. Yang, G. Jakob, Y. Mokrousov, and

M. Kläui, Harnessing orbital-to-spin conversion of interfacial orbital currents for efficient spin-orbit torques, Phys. Rev. Lett. **125**, 177201 (2020).

[54] S. Ding, Z. Liang, D. Go, C. Yun, M. Xue, Z. Liu, S. Becker, W. Yang, H. Du, C. Wang, Y. Yang, G. Jakob, M. Kläui, Y. Mokrousov, and J. Yang, Observation of the orbital Rashba-Edelstein magnetoresistance, Phys. Rev. Lett. **128**, 067201 (2022).

[55] G. Sala and P. Gambardella, Giant orbital Hall effect and orbital-to-spin conversion in 3d, 5d, and 4f metallic heterostructures, Phys. Rev. Res. **4**, 033037 (2022).

[56] V. P. Amin, J. Zemen, and M. D. Stiles, Interface-generated spin currents, Phys. Rev. Lett. **121**, 136805 (2018).

[57] G. Bihlmayer, P. Noël, D. V. Vyalikh, E. V. Chulkov and A. Manchon, Rashba-like physics in condensed matter, Nat. Rev. Phys. **4**, 642 (2022).